Appl Phys B (2009) 97: 897–908
DOI 10.1007/s00340-009-3761-z

Applied Physics B
Lasers and Optics

Characterization of fluctuating hydroxyl concentrations in a turbulent nonpremixed hydrogen–nitrogen jet flame

J. Zhang · G.B. King · N.M. Laurendeau

Received: 22 March 2009 / Revised version: 10 August 2009 / Published online: 23 October 2009

Abstract Two-point OH time-series measurements using a high-speed, laser-induced fluorescence system have been performed in a turbulent nonpremixed jet flame to obtain both radial and axial space–time correlations. Turbulent OH structures in such flames are found to undergo convection both axially and radially, but OH convection does not satisfy the 'frozen-turbulence' hypothesis owing to various turbulent interactions and chemical reactions. While axial OH convection occurs at approximately the local mean bulk velocity, radial convection is largely compromised by strong turbulent mixing along the same direction. The hydroxyl integral length scale can be interpreted as the typical dimension of a convective OH structure, which is axially elongated and becomes more isotropic in the post-flame region. The hydroxyl integral time scale can be interpreted as approximately the ratio of an axial integral length scale to a corresponding local mean flow velocity. In general, macroscale fluctuations of OH are dominated by large-scale turbulence, with little contribution from small-scale turbulence and OH chemistry.

PACS 32.50.+d · 47.70.Pq · 47.27.wg

J. Zhang (✉)
Combustion Research Facility (CRF), Sandia National Laboratories, MS 9052, P.O. Box 969, Livermore, CA 94551-0969, USA
e-mail: jzhang@sandia.gov
Fax: +1-925-2942276

J. Zhang · G.B. King · N.M. Laurendeau
School of Mechanical Engineering, Purdue University, West Lafayette, IN 47907-2088, USA

1 Introduction

Hydroxyl is an important intermediate species during combustion owing to its role in oxidation reactions as well as in formation of pollutants, such as NO and soot. As OH is strongly associated with high-temperature regions and is characterized by a strong fluorescence yield, it is often treated as a flame marker when studying turbulent combustion. Qualitative OH planar laser-induced fluorescence (PLIF), for instance, has been used to identify transitions from unburnt to burnt components [1], the fuel-lean side of reaction zones in diffusion flames [2], and flame–vortex interactions [3]. While OH is formed rapidly during combustion, it is consumed by relatively slow three-body recombination reactions and can thus survive for a fairly long time in low-temperature regions. For this reason, OH concentrations typically occur at superequilibrium levels [4] and exhibit larger spatial dimensions than actual flame zones [5], which is particularly the case for downstream locations within turbulent reacting jets. While this feature certainly compromises the utility of OH as a flame marker, the wide range of temporal and spatial scales for OH implies strong interactions with fluid turbulence [6]. The objective of this paper, therefore, is to characterize experimentally OH fluctuations and to provide a quantitative understanding of the associated turbulence–chemistry interactions.

Temporal fluctuations of OH have been previously investigated by our group for a number of turbulent nonpremixed jet flames [7]. The measurements [8] were obtained using a high-speed laser-induced fluorescence (LIF) technique called picosecond time-resolved laser-induced fluorescence (PITLIF). PITLIF can capture concentrations of radical species at rates of up to 20–40 kHz, thus resolving temporal macroscales of most laboratory-scale turbulent

flames. Temporal statistics for OH, including temporal autocorrelation functions, power spectral densities (PSDs) and integral time scales have been reported in previous work [7, 9]. The temporal statistics of OH were found to exhibit self-similarity in the far field of turbulent nonpremixed jet flames so that its integral time scale proved to be a good measure of macroscale fluctuations in OH concentration. By invoking time-series simulations based on state relationships for strained laminar flamelets, measured OH time series were used to derive integral time scales for mixture fraction, a very useful conserved scalar for turbulent nonpremixed combustion [9].

Though PITLIF has proven to be a powerful tool, as a single-point technique, it provides no information on the spatial features of a turbulent scalar field. Recently, however, we developed a two-point version of PITLIF which permits measurements of both spatial and temporal fluctuations in OH concentration by simultaneously monitoring two probe volumes [10, 11]. In the first implementation of this new approach, we used a single horizontal laser beam; hence, the separation between the two probe volumes was limited along the beam, which was typically the radial direction in the case of a round jet. A full characterization of OH fluctuations obviously requires two-point statistics along other directions. Considering the axisymmetry of the round jet, the remaining direction of importance is the axial direction, which necessitates a different laser configuration.

High-speed OH PLIF is another technique capable of monitoring fluctuating OH structures within turbulent flames. Recently, repetition rates of several kHz have been demonstrated, thus revealing dynamic flame phenomena, including local extinction and re-ignition [12–14]. Compared to two-point PITLIF, high-speed PLIF offers much richer information on two-dimensional OH distributions, such as orientation and thickness. Moreover, as a surrogate for the reaction zone, this OH PLIF technique can be applied simultaneously with two-dimensional velocity measurements, using particle image velocimetry (PIV), to investigate turbulence–flame interactions [15]. However, despite these advantages, high-speed OH PLIF is often hampered by its prohibitive cost and complexity. Furthermore, high-speed PLIF remains largely qualitative as corrections for collisional quenching are typically necessary on a shot-by-shot basis.

In this paper, we describe substantial improvements to the previous two-point PITLIF methodology so as to accommodate both radial and axial two-point separations. This improved two-point PITLIF technique is then employed to study OH fluctuations in a well-investigated turbulent hydrogen–nitrogen nonpremixed jet flame. When analyzing the measured statistics, we emphasize, in particular, differences between the radial and axial two-point statistics, including their underlying physics.

2 Experimental overview

2.1 Two-point PITLIF system

The laser system is nearly identical to that used in [7, 8, 10, 11]. In brief, the PITLIF technique employs a high repetition-rate UV laser for excitation and detection of OH. To produce such a beam, a mode-lock Ti:Sapphire laser at a repetition rate of 80 MHz is pumped by a 532-nm diode-pumped continuous-wave laser at 13.5 W; the generated IR pulsed beam is then frequency-tripled into the UV. The output UV laser pulse has a temporal width of 2 ps and a spectral width of 0.3 nm. Its wavelength is centered at 306.5 nm to selectively excite multiple transitions in the $(v' = 0,\ v'' = 0)$ vibrational band of the $A^2\Sigma^+ - X^2\Pi_i$ electronic system of OH. This excitation wavelength offers a minimal temperature dependence of the overall Boltzmann fraction over our temperature range (1500–2500 K), so that quenching-corrected fluorescence signals can be directly converted to OH concentrations [8].

The optical detection system is the same as that used in the first version of PITLIF [11]. Fluorescence generated from two probe volumes are first collected by an aspherical lens, then split by a UV beamsplitter, and eventually focused by spherical lens doublets onto corresponding detector assemblies, with each consisting of a monochromator and a photomultiplier tube. The monochromator serves as a narrow band-pass filter to accept fluorescence photons centered at 306.5 nm with a bandwidth of 10 nm. The entrance slit of each monochromator defines the location of the corresponding probe volume; translating one detector while keeping the other one fixed changes the separation distance between the two probe volumes. This optical detection system offers an overall magnification ratio of 1.19 and an f-number of 2.8. The signal received by each detector is a pulse train, with each pulse corresponding to a detected fluorescence photon and the time-varying pulse rate representing the temporal fluorescence decay. These signals are quantized using two gated photon-counting systems and later post-processed to produce concentration time series by correcting on-the-fly for electronic quenching, as explained in detail in [8, 10].

While a single horizontal laser beam is sufficient for radial two-point measurements [11], axial two-point measurements require either a single vertical laser beam or two horizontal beams with adjustable vertical separation. For ease of operation, we have adopted a two-beam configuration. Figure 1 shows the experimental layout for implementing such a two-beam system, together with the coordinate system for a jet flame. A linearly polarized UV beam generated from the laser system is first converted into a circular polarized laser with a zero-order quarter waveplate (¼λ), and then split into two beams ("P" and "S") with different polarizations within a 12.7-mm cube polarizing beamsplitter (BS).

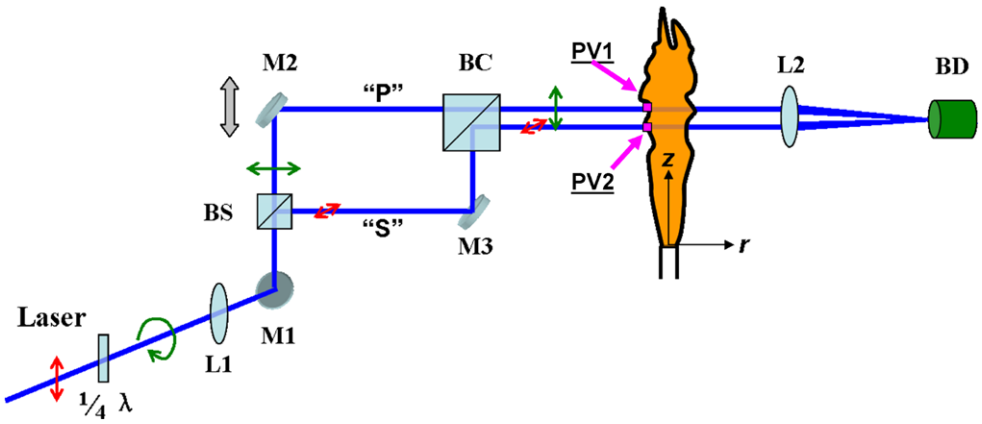

Fig. 1 Schematic of the two-beam system used for two-point PITLIF measurements: ¼λ, zero-order quarter waveplate; M, mirror; BS, polarizing cube beamsplitter; BC, polarizing cube beamsplitter used as beam combiner; PV, probe volume; L, lens; BD, beam dump. The *red* and *green arrows* identify the polarization; "P" and "S" designate the two split laser beams based on their polarizations. With this two-beam configuration, two probe volumes (PV1 and PV2) can have an axial offset Δz (as shown here), a radial offset Δr along one laser beam, or both

Table 1 Mean and standard deviation of hydroxyl concentration, time-averaged fluorescence lifetime ($\bar{\tau}$), and sampling rate (f) at measurement locations. The Batchelor frequency (f_B) and length scale (λ_B) are computed in [11]. $f/2 \geq f_B$ should be satisfied in order to resolve the Batchelor frequency

Location		Mean [OH]	$\sigma_{[OH]}$	$\bar{\tau}$	f_B	λ_B	f
z/D	r/D	(10^{-8} moles/cm^3)	(%)	(ns)	(kHz)	(μm)	(kHz)
10	1.19	1.78	82.6	1.38	7.5	263	12.5
20	1.53	0.92	109.6	1.52	6.0	363	10
30	1.57	0.75	108.2	1.53	4.1	514	8
30	0	0.41	133.6	1.54	5.5	514	6.25
33	0	0.59	114.2	1.51	3.9	631	8
35	0	0.67	99.2	1.50	3.1	727	10
40	0	0.56	94.0	1.34	2.2	830	8
45	0	0.26	130.7	1.20	1.5	982	6.25

The two split beams are subsequently folded with mirrors (M2 and M3) and recombined with a beam combiner (BC) to form two parallel horizontal beams across the flame. The beam combiner is actually another polarizing cube beamsplitter with an edge length of 25.4 mm. The axial two-point separation can be continuously adjusted by translating mirror M2. To assure consistent daily performance, all optical components except the waveplate and lenses are mounted on a 30 cm × 30 cm, vertically placed optical breadboard. This arrangement of two horizontal laser beams offers freedom for various two-point measurements, in that the separation between the two probe volumes (PVs) can be either radial, axial or both.

The temporal resolution of this improved two-beam system is $2/f$, where f is the sampling rate used during our experiments. A higher sampling rate resolves more high-frequency components within the turbulent field; however, the cost is a degradation of the signal-to-noise ratio. In practice, a compromise is made such that only the highest frequencies of interest are resolved for any experiment. Typically, as listed in Table 1, we choose sampling rates high enough to resolve the Batchelor frequency, the so-called dissipative frequency for scalars (such as species concentration) in turbulence. While such a high sampling rate is unattainable at some measurement locations, a slightly lower rate still resolves macroscale fluctuations thus producing accurate space–time statistics [11]. A complete discussion concerning the influence of sampling rate on our measured statistics can be found in [11].

The spatial resolution of any two-point system depends not only on the size of the probe volumes, but also on optical aberrations of the collection optics. For our current system, the dimension of both probe volumes is 350 × 350 × 210 μm^3, which is defined by the laser-beam diameter (e^{-2}) and the monochromator entrance-slit width. Unfortunately, aberrations associated with the optical configuration can lead to blurring of the focused images. The implication is that images from two nearby probe volumes may partially

overlap, thus generating artificial correlations in the measurements and limiting the smallest measurable two-point separation [11]. Even for two probe volumes having a large separation, for which image overlap may not be an issue, a detector may still receive a fluorescence signal other than from its intended probe volume. By a judicious selection of collection lenses, with the aid of software for optical design, we have minimized optical aberrations for this system [11]. An aberration-limited blur spot of less than 180 μm is achieved for a probe volume up to 6 mm away from the primary axis; the blur spot may deteriorate to 400 μm when the probe volume moves beyond 10 mm from the primary axis [15]. For all measurements, both probe volumes are kept within 10 mm of the primary axis; hence, the overall spatial resolution is around 350 μm, which can resolve the Batchelor length scale at most locations within our jet flame (Table 1).

The current two-beam configuration warrants further consideration concerning potential interferences between these two laser beams. When the two beams are sufficiently close, the fluorescence signal generated by each beam can enter the same detector. As fluorescence is randomly polarized, we have no means of rejecting photons generated from the unwanted beam; the result is false correlation, the same problem caused by excessive optical aberrations. Experimentally, we can determine the range for possible two-beam interferences by examining the change in time-averaged signal at a fixed detector while varying the axial two-point separation, Δz, between the two laser beams. For all measurements, the interference range beyond which the signal experiences little variation is between -1.0 and 0.5 mm, where the negative and positive signs correspond to upstream and downstream directions, respectively.

Although reducing the entrance-slit height of the monochromators can help narrow the interference range, we find that too tight a slit risks missing focused signal owing to beam steering effects within turbulent flames. To account for potential two-beam interferences, we use only one laser beam for radial two-point measurements; when two beams are inevitable during axial two-point measurements, we reject measurements within the interfering Δz range. We note that these rejected points correspond to small scales within the flow, such as the Batchelor scale and the Taylor microscale. Fortunately, lack of information at these small scales does not have a significant impact on measured integral length scales, with a typical uncertainty of less than 5%. Such interferences could be avoided, by the way, if a similar two-beam alignment were adopted for Rayleigh or Raman scattering measurements, as the generated signal photons possess the same polarization as the excitation laser and can thus be conveniently differentiated by inserting a polarizer in front of the detector.

2.2 Combustor and flame configurations

The combustor for this study is a simple round-jet burner, similar to that used by Bergmann et al. [5]. A long 8-mm diameter tube with a thinned rim at the exit is used to supply fuel and a concentric 140-mm diameter contoured nozzle is used to provide co-flowing air at a velocity of 0.2 m/s. The whole burner sits on a translation system and can be moved in both the radial and axial directions to change measurement location.

The flame under study has a fuel composition of 50% H_2/ 50% N_2 (by volume) and a Reynolds number of 10,000. Designated as H3, this flame has undergone many experimental investigations in the past, including Raman [16], Raman/LIF [17] and LDV/CARS/Raman measurements [18], and has been chosen as a benchmark for the International Turbulent Nonpremixed Flame (TNF) workshops [19]. Such comprehensive single-shot data from past work lay a solid foundation for our later interpretation of the two-point OH time series of this investigation.

2.3 Experimental procedure and data analysis

Both axial and radial two-point measurements of hydroxyl concentration are obtained at the same locations as [11]. These include three radial peak [OH] locations and five axial locations, with z/D ranging from 10 to 45, where $z/D = 35$ corresponds to the time-averaged stoichiometric flame tip. At each measurement location, separation distances between the two probe volumes typically varied from -6.0 to 6.0 mm for radial two-point measurements (Δr), and from -10 to 10 mm for axial two-point measurements (Δz). A larger range for Δz is used because scalar structures within jet flames have been found to be slightly elongated along the axial direction [20]. At each two-point separation, fifty time series of 8192 samples each were collected to build reliable statistics. The measured data are converted to concentrations and fluorescence lifetimes using the method developed by Renfro et al. [21], thus accounting for nonlinear operation of the discriminators at high photon-count rates. The resulting concentration time series are then analyzed to compute relevant statistics, where corrections for the effects of random noise are made via the method previously developed by Zhang et al. [11].

A number of statistics having practical significance can be derived from two simultaneous time series of OH concentration. The Eulerian space–time correlation is given by

$$f_{ST}(\Delta\vec{r}, \Delta t; \vec{r}) = \frac{\overline{c'(\vec{r}, t)c'(\vec{r} + \Delta\vec{r}, t + \Delta t)}}{[\overline{c'(\vec{r}, t)^2} \cdot \overline{c'(\vec{r} + \Delta\vec{r}, t + \Delta t)^2}]^{1/2}}, \quad (1)$$

where $c'(\vec{r}, t)$ is the fluctuating component of OH concentration at location $\vec{r}$ and time t. This particular function characterizes the correlation between two scalar values at spatial

separation $\Delta\vec{r}$ with temporal delay Δt; $\Delta\vec{r}$ takes the form Δr or Δz for radial or axial two-point separations, respectively. The space–time correlation contains information concerning both length and time scales. As special cases of the space–time correlation, the spatial autocorrelation function, given by

$$f_S(\Delta\vec{r};\vec{r}) = f_{ST}(\Delta\vec{r},\,\Delta t = 0;\vec{r}), \tag{2}$$

and the temporal autocorrelation function, given by

$$f_T(\Delta t;\vec{r}) = f_{ST}(\Delta\vec{r} = 0,\,\Delta t;\vec{r}), \tag{3}$$

retain only spatial and temporal information, respectively. Integral length and time scales, characterizing the most energetic fluctuations, are defined from these autocorrelation functions as

$$l_I(\vec{r}) = \int_0^\infty f_S(\Delta\vec{r};\vec{r})\,d(\Delta\vec{r}) \tag{4}$$

and

$$\tau_I(\vec{r}) = \int_0^\infty f_T(\Delta t;\vec{r})\,d(\Delta t), \tag{5}$$

respectively.

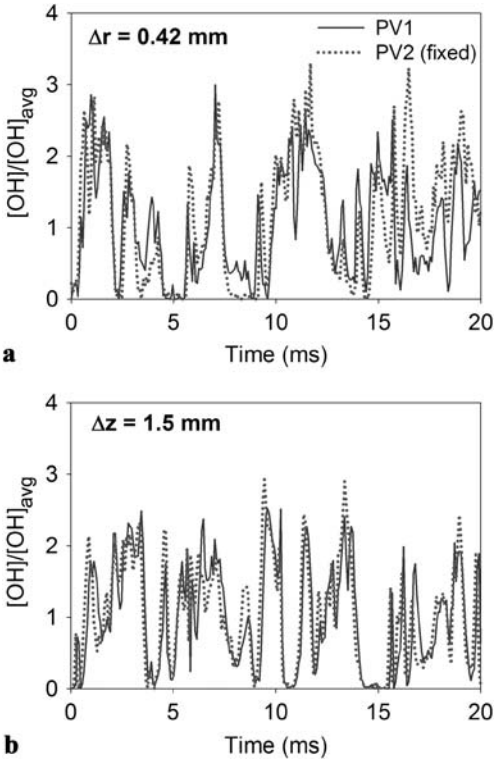

Fig. 2 Sample [OH] time series at $z/D = 10$ for the H3 flame from (**a**) radial and (**b**) axial two-point measurements. Positive Δr and Δz represent two-point separations along the air side and the downstream direction, respectively

3 Results and discussion

Table 1 lists measured mean OH concentrations and fluorescence lifetimes at all measurement locations. The current radial positions corresponding to peak [OH] locations are slightly different from those reported in previous measurements [11]; the deviations, all within 1.5 mm, arise from the uncertainty in determining radial peaks from time-averaged radial [OH] profiles. In general, the mean OH concentration decreases with downstream position at the peak radial [OH] locations. This behavior is consistent with the observations of Drake et al. [22] and represents the combined result of reduced superequilibrium and more agitated flame motion at downstream locations. Along the jet centerline, the mean OH concentration peaks at $z/D = 35$, which corresponds to the stoichiometric flame tip.

3.1 Radial and axial two-point statistics

Typical two-point time series for [OH] are shown in Fig. 2 for the H3 flame at 10 jet diameters downstream from the nozzle ($z/D = 10$). In Fig. 2(a), the two probe volumes are separated by 0.42 mm along the radial direction of the jet. As expected, these two time series show a certain degree of resemblance, indicating a spatial correlation. A similar resemblance is observed for the axial two-point time series, but at a much larger separation distance of 1.5 mm (Fig. 2(b)), suggesting a longer correlation range than for the radial coordinate. For both directions, the similarity between simultaneous time series disappears at large two-point separations.

The corresponding space–time correlations derived from the axial two-point time-series measurements are shown in Fig. 3. The general trend for the Eulerian two-point, two-time correlations is a reduction from one to zero as Δt and Δz increase, with one being perfectly correlated and zero being totally uncorrelated in concentration fluctuations. Several features can be identified from these space–time correlations. First, for nonzero Δz, i.e., for the non-fixed probe volume located either upstream or downstream of the fixed probe volume, the maximum of each correlation curve occurs at nonzero time delay. A similar phenomenon has been observed for streamwise space–time correlations of velocity [23] and temperature [24] in nonreacting flows and for those of temperature in premixed jet flames [20], both considered characteristic of turbulent structures under convection along a given direction. In our case, this same feature occurs because OH structures are convected downstream. Hence, the convection time between the two probe volumes is closely related (if not equal) to the time delay corresponding to the maximum correlation.

Second, the correlation peak falls progressively below unity with an increasing magnitude in axial two-point sep-

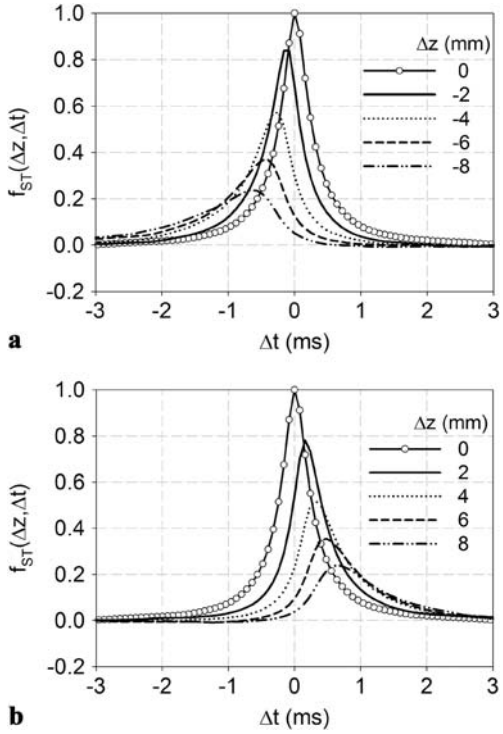

Fig. 3 Space–time correlations of [OH] fluctuations for axial two-point separations at the radial peak [OH] location and $z/D = 10$. Negative Δz corresponds to the upstream direction and vice versa. Data points are included only for $\Delta z = 0$ to avoid cluttering of correlation curves

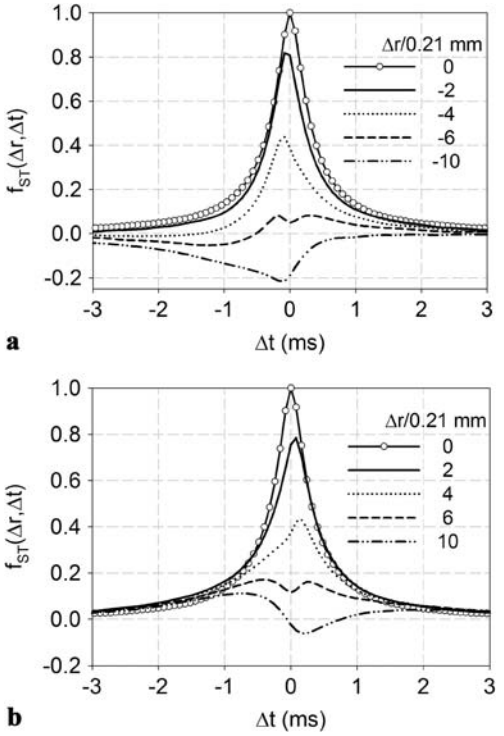

Fig. 4 Space–time correlations of [OH] fluctuations for radial two-point separations at the radial peak [OH] location and $z/D = 10$. Negative Δr corresponds to the fuel side and positive Δr to the air side. Data points are included only for $\Delta r = 0$ to avoid cluttering of correlation curves

aration. This behavior indicates that the OH structures are transported in a "non-frozen" manner since frozen turbulence, or Taylor's approximation, will lead to constant maxima in the two-point, two-time correlations. In general, reductions in peak Eulerian correlations can be caused by turbulent mixing at various length scales, namely, distortion of turbulence by mean shear, local production of turbulence, turbulent diffusion, and viscous dissipation [25]. For reactive scalars, such as OH, chemical reactions can act as either source or sink, and are thus another complication whose significance might be evaluated using similarly defined Damköhler numbers [4]. Whatever the exact mechanism, the scalar OH structure can be imagined as a pocket of "property particles" [25], which undergoes modification during convection and thus changes from its original form; the longer the distance traveled, the greater the difference in evolving structure.

Comparisons of space–time correlations between those having positive and negative Δz's suggest that this correlation is generally not symmetric with respect to spatial separation. Nevertheless, over short distances compared to the correlation length,

$$f_{ST}(\Delta z, \Delta t; z) \approx f_{ST}(-\Delta z, -\Delta t; z), \tag{6}$$

as shown in Fig. 3. This approximate symmetry is remnant of the relationship

$$f_{ST}(\Delta z, \Delta t; z) = f_{ST}(-\Delta z, -\Delta t; z + \Delta z), \tag{7}$$

which may be proved by switching the two probe volumes of (1).

Figure 4 shows radial space–time correlations determined at the same location as for Fig. 3. Features similar to the axial space–time correlations are observed, including asymmetry between positive and negative Δr's and a shifting maximum correlation at nonzero Δr's. The latter suggests an overall radial convection of fluctuating OH structures from the fuel side to the air side. In comparison to the axial direction, radial OH convection is less obvious, with the correlation curves peaking very close to $\Delta t = 0$. Moreover, the correlation peak demonstrates more drastic decay with increasing two-point separation, suggesting a greater departure from frozen turbulence. Further discussion concerning this difference is deferred to Sect. 3.2.

From Fig. 4, we also note that a significant negative correlation exists for large two-point separations on the fuel side, e.g., $\Delta r = -2.1$ mm at $\Delta t = 0$, which is not found at other downstream locations. This negative correlation indicates that OH concentrations at such displacements generally fluctuate in the opposite manner for the two probe

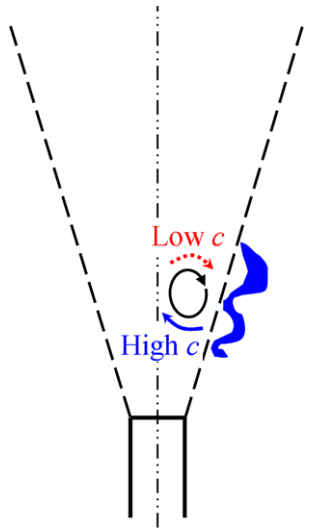

Fig. 5 Schematic of proposed interactions between the OH layer and inner coherent vortices at low flame heights. The *red dashed* and *blue solid arrows* identify inward and outward fluid motions with respect to the OH layer, respectively. The *dashed* lines show the boundary of the shear layer

volumes. Such negative correlations have been previously found for lateral correlations of longitudinal velocity [26] and temperature [27] in plane jets, which is typically attributed to spanwise vortices arranged on the opposite sides of the jet centerline. In a similar fashion, we propose that the negative correlation in our case is caused primarily by coherent vortices located on the fuel side of the flame front, the existence of which has been corroborated by planar reactive-Mie-scattering within various turbulent jet flames [28].

As shown schematically in Fig. 5, for a fixed probe volume at the mean [OH] peak, an inward motion of these coherent vortices with respect to the [OH] peak introduces fluid parcels with low OH concentrations, thus causing negative concentration fluctuations at this fixed probe volume. Likewise, an outward motion results in positive concentration fluctuations some distance away. Therefore, fluctuations in OH concentration become negatively correlated as the probe volume shifts sufficiently far away from the [OH] peak. The fact that these organized vortical structures are only present near the flame base within a turbulent jet flame also explains the absence of negative correlations at other downstream locations. Clearly, our proposition of coherent vortices requires further tests, possibly via jet flames with varying Reynolds number.

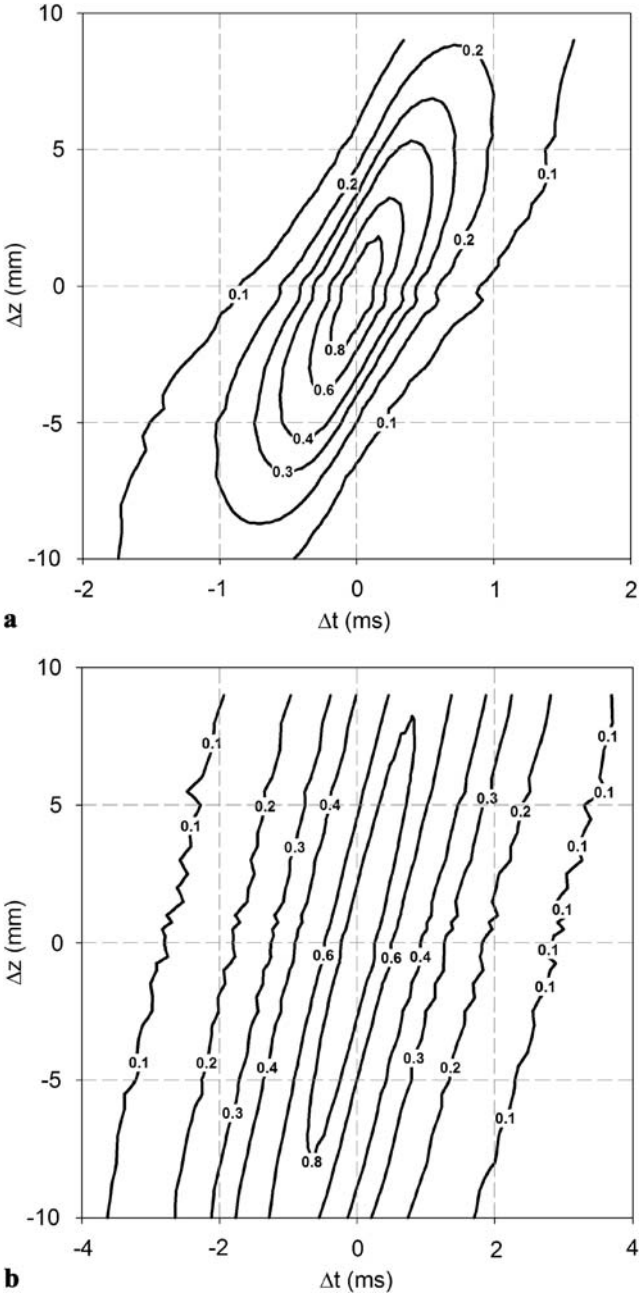

Fig. 6 Space–time correlation maps of [OH] fluctuations for two-point separations along the axial direction at (**a**) the radial [OH] peak for $z/D = 10$ and (**b**) the jet axis for $z/D = 45$. Negative Δz corresponds to the upstream direction and vice versa

3.2 Taylor's hypothesis and convection of OH structures

Convection of turbulence and any associated scalar structures stems from Taylor's original hypothesis on grid turbulence. According to Taylor [29], at low turbulence levels the spatial pattern of fluctuating velocity is rigidly translated to other locations at the mean-flow velocity; hence,

$$f_{ST}(\Delta z, \Delta t) = f_{ST}(\Delta z + V_C \tau_1, \Delta t + \tau_1), \tag{8}$$

where the convection velocity, V_C, is assumed to be equal to the mean velocity. This hypothesis, the so-called "frozen-turbulence approximation," is only accurate for grid generated turbulence at small turbulence intensities, and is not strictly valid for free shear flows, such as jets [30]. Indeed, space–time correlations based on measured OH concentrations in our investigation demonstrate non-frozen transport of OH structures within a jet. To explore this idea further, we exploit a constant space–time correlation map.

For an ideal Taylor's model, constant space–time correlations satisfying (8) would be depicted in the $(\Delta z, \Delta t)$-plane

Table 2 Axial and radial turbulent intensities, mean axial velocity and OH convection velocity at measurement locations. Turbulent intensities are computed from [18] but are not available at some locations owing to a lack of rms velocity data. V and W are axial and radial velocities, respectively. The convection velocities are determined from (9)

Location		$V_{\text{rms}}/V_{\text{mean}}$	$W_{\text{rms}}/W_{\text{mean}}$	V_{mean}	V_C
z/D	r/D			(m/s)	(m/s)
10	1.19	–	–	12.4	14.5
20	1.53	0.46	1.65	13.7	15.1
30	1.57	–	–	13.2	13.8
30	0	0.24	–	17.6	17.2
33	0	0.26	–	15.5	15.7
35	0	0.29	–	14.1	15.1
40	0	0.29	–	11.4	13.3
45	0	0.30	–	9.2	11.7

as parallel lines with a slope equal to the convection speed, V_C, indicating rigid convection of scalar structures at constant velocity. Figure 6 presents axial space–time correlation maps of OH concentration at two locations within the H3 flame: one at the mean [OH] peak for $z/D = 10$ and the other at the jet axis for $z/D = 45$. For both locations, these correlation maps retain some features of Taylor's hypothesis. The constant correlation lines are approximately parallel to each other over a narrow range of two-point separations; however, they eventually close within the large Δz region, confirming a non-rigid convection of OH structures within reacting jets.

Compared with the radial peak [OH] location at $z/D = 10$, the space–time correlation on the jet axis for $z/D = 45$ shows a greater resemblance to an ideal Taylor's model (Fig. 6). In fact, for all measurements of this study, axial space–time correlations along the jet axis more closely approach Taylor's ideal case than those away from the centerline. As mentioned earlier, non-frozen transport of turbulent OH structures arises from a number of factors, including turbulent mixing and chemical reactions. The intensity of turbulent mixing can be evaluated from the axial turbulent intensity, defined by $V_{\text{rms}}/V_{\text{mean}}$. From the limited velocity data available in the literature [18], we find that this turbulent intensity is indeed greater at radial [OH] peaks as compared to the jet centerline (Table 2). Axial transport across the radial [OH] peaks should also experience more vigorous chemical reactions involving OH, as compared to transport along the jet centerline, since the mean radial [OH] peaks are located close to the stoichiometric contour. We should point out, however, that while time-averaged fluid advection at the jet axis is predominantly in the axial direction, that at the radial [OH] peaks includes a minor radial component, which should produce a further departure from the ideal Taylor's case for OH transport.

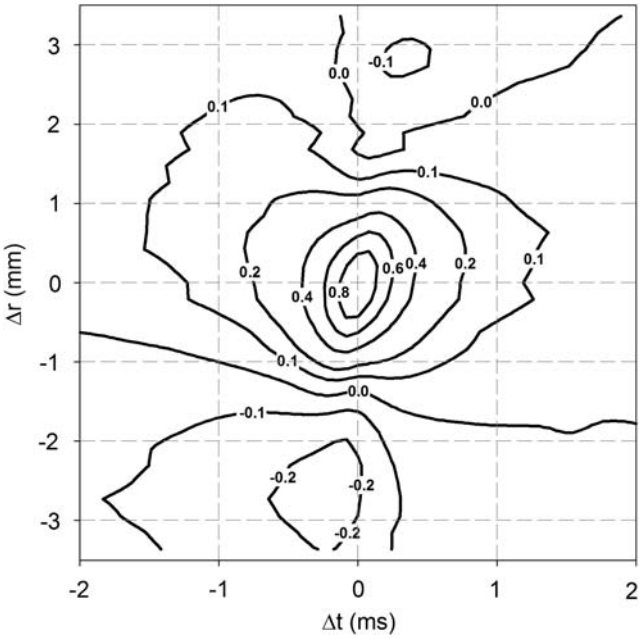

Fig. 7 Space–time correlation maps of [OH] fluctuations for two-point separations along the radial direction at the radial [OH] peak for $z/D = 10$. Negative Δr corresponds to the fuel-side direction and positive Δr to the air-side direction

Figure 7 depicts radial space–time correlation maps at the radial [OH] peak for $z/D = 10$. In contrast to correlation maps for axial two-point separations, as shown in Fig. 6, the correlation maps for radial two-point separations are devoid of any convective pattern and show more symmetry between positive and negative Δr values. As indicated by Table 2, axisymmetric jets typically display larger radial velocity fluctuations (W_{rms}) as compared to mean radial velocities (W_{mean}), thus producing strong radial turbulent intensities ($W_{\text{rms}}/W_{\text{mean}}$). Consequently, OH structures under radial convection would be expected to undergo much stronger turbulent mixing than those under axial convection.

Even though Taylor's hypothesis is not strictly correct, steady convection of turbulent eddies and accompanying scalar structures is apparently a prevalent concept. The convection velocity, which may not necessarily be the mean-flow velocity, can be defined here as the two-point separation divided by the time delay corresponding to the maximum correlation, i.e.,

$$V_C = \frac{\Delta z}{\tau_d}, \tag{9}$$

where the delay time τ_d can be described mathematically as

$$\partial f_{ST}(\Delta z, \Delta t)/\partial(\Delta t)\,\big|_{\Delta t=\tau_d} = 0. \tag{10}$$

A cubic spline can be fitted to the correlation curve $f_{ST}(\Delta z, \Delta t)$ to find the delay time, τ_d, through (10). Calculated convection velocities at the radial peak [OH] location for $z/D = 10$ are shown in Fig. 8 for various two-point

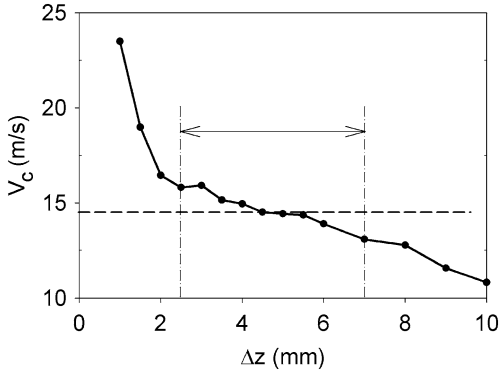

Fig. 8 Convection velocity of OH structures estimated from space–time correlations for various two-point separation distances at the radial peak [OH] location and $z/D = 10$. The effective convection velocity is defined as an average (the *dashed line*) after discarding the first and last three points to avoid errors resulting from truncation and curve-fitting

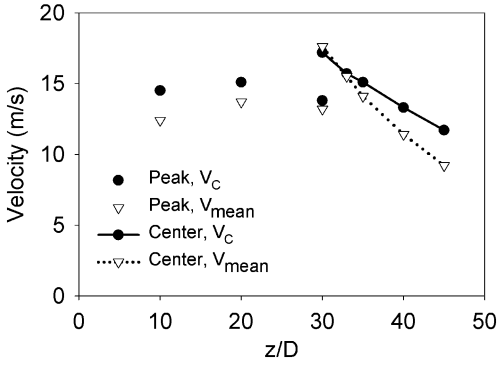

Fig. 9 Comparison of OH axial convection velocity (V_C) and mean axial dynamic velocity [18] at measurement locations corresponding to the mean radial [OH] peak and the jet centerline

separations. Clearly, the convection velocity depends somewhat on the choice of two-point separation. This ambiguity in convection velocity has been noted previously for velocity measurements in nonreacting jets [23]. Variable choices, including the wavenumber, have been proposed to achieve consistency; however, such procedures shed little light on the underlying physics. For this investigation, we define the effective convection velocity as the average of convection velocities at different two-point separations. However, values are discarded at small and large separations, as such calculations are likely contaminated owing to truncation errors at small separations and errors associated with curve-fitting at large separations.

Figure 9 shows effective axial convection velocities at various measurement locations. Previously measured mean axial velocities in the same flame [18] are plotted for comparison. In general, the OH convective velocity is quite consistent with the mean bulk velocity, particularly at $z/D =$ 30–35. The biggest discrepancy occurs at the jet centerline in the post-flame region ($z/D = 45$). Consistency between the convection velocity and mean-flow velocity has previously been found for thermal structures within premixed jet flames [20]. Compared with temperature, the OH concentration is obviously a more reactive scalar and thus has usually been considered to be a relatively faster scalar. Therefore, we should not be too surprised that large-scale OH variations along the vertical direction appear to be largely controlled by the dynamic flow field.

Previous measurements of the scalar dissipation rate have often evoked Taylor's hypothesis and assumed that the scalar gradient, or a specific component, can be reconstructed from a single-point time series as [31, 32]

$$\frac{\partial c}{\partial z} \simeq \frac{1}{V_{\text{mean}}} \cdot \frac{\partial c}{\partial t}, \tag{11}$$

Table 3 Hydroxyl integral length and time scales. The ratio between the axial and radial integral length scales provides a measure of the aspect ratio for convective OH structures

Location		$l_{I,z}$	$l_{I,r}$	$l_{I,z}/l_{I,r}$	τ_I
z/D	r/D	(mm)	(mm)		(ms)
10	1.19	3.1	0.7	4.4	0.40
20	1.53	3.2	1.4	2.3	0.37
30	1.57	3.9	1.9	2.1	0.43
30	0	4.7	2.8	1.7	0.32
33	0	4.4	2.7	1.6	0.34
35	0	4.1	2.7	1.5	0.32
40	0	5.3	4.2	1.3	0.65
45	0	8.4	7.7	1.1	1.16

where c is the measured scalar. In the context of our study, this assumption should obviously be used with caution, as the scalar convective velocity may not be the same as the corresponding mean flow velocity. Similar two-point, time-series measurements of the scalar of interest are clearly necessary to evaluate the validity of (11).

3.3 Integral scales for OH

The spatial and temporal integral scales for fluctuating OH concentration, as listed in Table 3, are computed according to (4) and (5). Measurements of the radial integral length scale, $l_{I,r}$, and the integral time scale, τ_I, are not unique to the improved two-beam PITLIF technique and have been reported previously using a single-beam setup [11]; nevertheless, they are included here to provide a complete picture of OH fluctuations. We note that the axial length scales are consistently greater than the radial length scales, especially near the flame base. Beyond the flame tip, the two length scales start to approach one another.

We have shown earlier that fluctuations in OH concentration for turbulent jet flames can be interpreted as the convection of turbulent OH structures accompanied by various alterations from turbulence and chemical reactions. From this perspective, the integral length scale, which characterizes the most energetic fluctuations, can be taken as the characteristic dimension of the OH structures under convection. Hence, the difference between the integral scales along the axial and radial directions suggests that the OH structures tend to be axially elongated, as for thermal structures in a similar round-jet system [20]. Moreover, near the flame base, these structures have a very high aspect ratio, with $l_{I,z}/l_{I,r} > 4$ at $z/D = 10$, which is consistent with prior observations of thin OH filaments via PLIF imaging [5, 33]. Marching downstream, the OH structures become more isotropic in the r–z plane, which comports well with the observed thickening, wrinkling, and eventual merging of OH zones [33].

Hydroxyl integral length scales along the axial and radial directions display distinct trends within the jet flame. At mean [OH] peaks, $l_{I,r}$ has been observed to rise almost linearly with increasing z/D [11], while $l_{I,z}$ exhibits a very modest rise with increasing distance from the nozzle (Table 3). In view of the corrugated OH layer near the flame front, we can interpret the radial integral length scale as the typical lateral dimension of a corrugated OH layer. Below the flame tip, corrugation of the OH layer is primarily controlled by local turbulence [34]; hence, the lateral length scale is dictated by the average eddy size, which is proportional to the jet width δ and thus to the axial distance in a jet flame; i.e.,

$$l_{I,r} \sim l_{\mathrm{OH}} \sim \delta(z) \sim z/D, \tag{12}$$

where l_{OH} is the lateral OH corrugation scale and the effect of a virtual origin has been intentionally neglected. Although $l_{I,z}$ can be similarly treated as a typical vertical dimension of the OH structures, a similar scaling relation cannot be easily obtained, especially considering the continuous pattern of OH structures along the vertical direction. As we found earlier in Sect. 3.2, large-scale variations in [OH] along the axial direction are primarily determined by the bulk flow, so that $l_{I,z}$ is probably closely related to the longitudinal integral scale for axial velocity.

Along the jet centerline, both $l_{I,z}$ and $l_{I,r}$ vary little below the flame tip and increase rapidly beyond the flame tip. In this region, the OH zone exists essentially as a diffuse field resulting from the merging of convoluted OH layers. Therefore, the lack of defined OH structures clearly requires a different interpretation for the OH integral scales other than the previous corrugation scales. Furthermore, it is reasonable to presume that OH has the same integral length scale as other broadly distributed scalars in this region, such as temperature and mixture fraction, which are both closely related to the dynamic length scale. However, with limited velocity data available, it is beyond the scope of this paper to seek such a scaling relation.

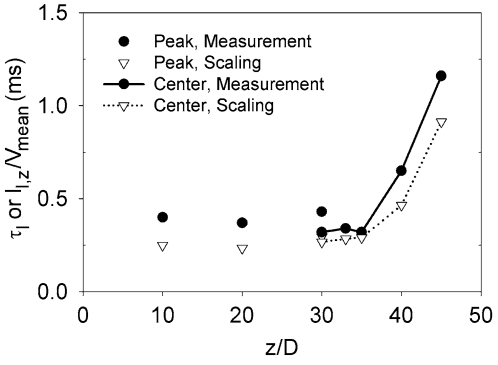

Fig. 10 Comparison of measured OH integral time scale and its scaling relation at positions corresponding to the mean radial [OH] peak and the jet centerline

While the integral time scale based on velocity is the turnover time for the most energetic eddies [30], the OH integral time scale can be likewise interpreted as that time taken by typical OH structures to sweep through the location; hence,

$$\tau_I \sim l_{I,z}/V_{\mathrm{mean}}. \tag{13}$$

Figure 10 compares the measured hydroxyl integral time scale with its scaling relation based on (13). Not surprisingly, this overly simple relation does not faithfully predict the hydroxyl time scale; nevertheless, it provides a quite reasonable estimation since it displays the same trend with respect to axial location.

Having investigated the statistics of fluctuating OH concentrations, a question naturally arises about the relationship between such fluctuations and those of the corresponding flame front. As discussed previously, OH is always present in the reaction zone within flames; however, it typically occupies a larger region than the actual stoichiometric contour. Indeed, for this diluted hydrogen flame, the stoichiometric contour comports closely with the region of maximum OH concentration, as verified by laminar flamelet simulations for a wide range of strain rates. For this reason, we attempted to deduce the statistics of the flame sheet from measured OH time series [15]. This was done by comparing the OH concentration to a preset threshold value and defining the presence of a flame sheet in terms of OH concentrations above this threshold, thereby producing a time series for the flame sheet. Statistics derived from these time series suggest that the flame front motion and OH concentrations have almost the same two-point statistics, which is not totally surprising as the method for constructing the time series for the flame front essentially represents a low-pass filter. From the

perspective of flamelet theory, the flame corresponds to a stoichiometric mixture fraction and is mainly controlled by large-scale motion within the jet shear layer [6]; our results simply reaffirm the dominance of macroscale mixing in OH fluctuations. Though a potentially useful technique, our approach has obvious drawbacks, as the choice of threshold value is subjective, which becomes especially disputable in downstream regions of the flame, where OH containing regions are broad and are characterized by small gradients in concentration.

4 Conclusions

We have implemented a new two-beam configuration for our previous two-point PITLIF technique, which enables both radial and axial two-point, time-series measurements of minor species concentration. The two-beam laser configuration gives rise to signal interferences between the two probe volumes for small separation distances, which prevents resolution at the smallest spatial scales. However, the resolution issue is quite negligible for determination of macroscale statistics, including integral length scales.

This improved system has been used to characterize fluctuating OH concentrations within a standard turbulent nonpremixed jet flame. Both axial and radial space–time correlations exhibit a maximum with shifting time delay for different two-point separations, an indication of the overall convection of OH structures. Taylor's hypothesis does not strictly hold for OH convection in such jet flames because of various interactions, including turbulent mixing and combustion. The space–time correlations suggest that locations along the jet axis comport better with Taylor's ideal model than those off centerline, where turbulent mixing is more intense and chemical reactions are more vigorous. Axial convection velocities for OH structures are quite close to mean local flow velocities. Radial convection of OH structures, in contrast, is partly obscured by strong radial turbulent mixing. Radial space–time correlations exhibit significant negative values near the flame base, hinting at the existence of coherent vortices on the fuel side of the reaction zone.

By interpreting the axial OH integral length scale as a characteristic dimension of convective hydroxyl structures, we find that turbulent OH structures are axially elongated throughout the flame, but become more isotropic in the post-flame region. The radial OH length scale at mean [OH] peaks can be scaled to the mean eddy size and are thus found to increase proportionally with axial distance. The OH integral time scale can be approximately scaled as the ratio of an axial OH length scale to a mean bulk velocity.

In summary, for the H3 flame, OH space–time correlations prove sensitive to the effects of small-scale turbulence and OH chemistry. Nevertheless, OH macroscale characteristics, including the convection velocity, integral length scale and integral time scale, are determined primarily by large-scale turbulence.

Acknowledgements This project was supported by the Air Force Office of Scientific Research. Dr. Julian Tishkoff is cordially acknowledged for acting as technical monitor.

References

1. M.M. Tacke, D. Geyer, E.P. Hassel, J. Janicka, Proc. Combust. Inst. **27**, 1157 (1998)
2. J.M. Donbar, J.F. Driscoll, C.D. Carter, Combust. Flame **122**, 1 (2000)
3. C.F. Kaminski, J. Hult, M. Alden, Appl. Phys. B **68**, 757 (1999)
4. R.S. Barlow, R.W. Dibble, J.-Y. Chen, R.P. Lucht, Combust. Flame **82**, 235 (1990)
5. V. Bergmann, W. Meier, D. Wolff, W. Stricker, Appl. Phys. B **66**, 489 (1998)
6. N. Peters, *Turbulent Combustion* (Cambridge University Press, Cambridge, 2000)
7. M.W. Renfro, W.A. Guttenfelder, G.B. King, N.M. Laurendeau, Combust. Flame **123**, 389 (2000)
8. S.D. Pack, M.W. Renfro, G.B. King, N.M. Laurendeau, Opt. Lett. **23**, 1215 (1998)
9. M.W. Renfro, J.P. Gore, N.M. Laurendeau, Combust. Flame **129**, 120 (2002)
10. J. Zhang, K.K. Venkatesan, G.B. King, N.M. Laurendeau, M.W. Renfro, Opt. Lett. **30**, 3144 (2005)
11. J. Zhang, G.B. King, N.M. Laurendeau, M.W. Renfro, Appl. Opt. **46**, 5742 (2007)
12. W. Paa, D. Müller, H. Stafast, W. Triebel, Appl. Phys. B **86**, 1 (2007)
13. M.E. Cundy, V. Sick, Appl. Phys. B **96**, 241 (2009)
14. B. Böhm, C. Heeger, I. Boxx, W. Meier, A. Dreizler, Proc. Combust. Inst. **32**, 1647 (2009)
15. J. Zhang, Development of a two-point high-speed laser-induced fluorescence technique and its applications to turbulent jet flames for OH concentration. Ph.D. Thesis, Purdue University, West Lafayette, IN (2007)
16. W. Meier, S. Prucker, M.-H. Cao, W. Stricker, Combust. Sci. Technol. **118**, 293 (1996)
17. W. Meier, A.O. Vyrodov, V. Bergmann, W. Stricker, Appl. Phys. B **63**, 79 (1996)
18. D.G. Pfuderer, A.A. Neuber, G. Fruchtel, E.P. Hassel, J. Janicka, Combust. Flame **106**, 301 (1996)
19. R.S. Barlow, R.W. Bilger, J.-Y. Chen, I. Gökalp, E.P. Hassel, A.R. Masri, N. Peters, in *Proceedings of the 1st International Workshop on Measurements and Computation of Turbulent Nonpremixed Flames*, Naples, Italy (1996)
20. C. Ghenai, I. Gökalp, Exp. Fluids **24**, 347 (1998)
21. M.W. Renfro, S.D. Pack, N.M. Laurendeau, Appl. Phys. B **69**, 137 (1999)
22. M.C. Drake, R.W. Pitz, M. Lapp, C.P. Fenimore, R.P. Lucht, D.W. Sweeney, N.M. Laurendeau, in *Twentieth Symposium (International) on Combustion*, The Combustion Institute, Pittsburgh (1984), pp. 327–335
23. J.A.B. Wills, J. Fluid Mech. **20**, 417 (1964)
24. S. Tavoularis, S. Corrsin, J. Fluid Mech. **104**, 311 (1981)
25. J.O. Hinze, *Turbulence*, 2nd edn. (McGraw–Hill, New York, 1975)
26. J.C. Mumford, J. Fluid Mech. **118**, 241 (1982)
27. R.A. Antonia, L.W.B. Browne, S. Rajagopalan, A.J. Chambers, J. Fluid Mech. **134**, 49 (1983)

28. V.R. Katta, L.P. Goss, W.M. Roquemore, L.-D. Chen, Dynamics of propane jet diffusion flames, in *Atlas of Visualization III*. The Visualization Society of Japan (CRC Press, Boca Raton, 1997)
29. G.I. Taylor, Proc. R. Soc. Lond. Ser. A **164**, 476 (1938)
30. S. Pope, *Turbulent Flows* (Cambridge University Press, Cambridge, 2000)
31. Z. Warhaft, Annu. Rev. Fluid Mech. **32**, 203 (2000)
32. G.H. Wang, N.T. Clemens, P.L. Varghese, Proc. Combust. Inst. **30**, 691 (2005)
33. J.M. Seitzman, A. Ungut, P.H. Paul, R.K. Hanson, in *Twenty-Third Symposium (International) on Combustion*, The Combustion Institute, Pittsburgh (1990), pp. 637–644
34. R. Abu-Gharbieh, G. Hamarneh, T. Gustavsson, C. Kaminski, J. Math. Imaging Vis. **19**, 199 (2003)